8

THE FINITE-DIFFERENCE TIME-DOMAIN METHOD FOR NUMERICAL MODELING OF ELECTROMAGNETIC WAVE INTERACTIONS WITH ARBITRARY STRUCTURES

A. Taflove and K. R. Umashankar

8.1 Introduction

Accurate numerical modeling of full-vector electromagnetic wave interactions with arbitrary structures is difficult. Typical structures of engineering interest have shapes, apertures, cavities, and material compositions or surface loadings which produce near fields that cannot be resolved into finite sets of modes or rays. Proper numerical modeling of such near fields requires sampling at sub-wavelength resolution to avoid aliasing of magnitude and phase information. The goal is to provide a self-consistent model of the mutual coupling of the electrically-small cells comprising the structure.

This chapter reviews the formulation and applications of a candidate numerical modeling approach for this purpose: the finite-difference time-domain (FD-TD) solution of Maxwell's curl equations. FD-TD is very simple in concept and execution. However, it is remarkably robust, providing highly accurate modeling predictions for a wide variety of electromagnetic wave interaction problems. FD-TD is

analogous to existing finite-difference solutions of scalar wave propagation and fluid-flow problems in that the numerical model is based upon a direct, time-domain solution of the governing partial differential equation. Yet, FD-TD is a non-traditional approach to numerical electromagnetics for engineering applications where frequency-domain integral equation approaches have dominated for 25 years.

One of the goals of this chapter is to demonstrate that recent advances in FD-TD modeling concepts and software implementation, combined with advances in computer technology, have expanded the scope, accuracy, and speed of FD-TD modeling to the point where it may be the preferred choice for complex electromagnetic wave penetration, scattering, guiding, and inverse scattering problems. With this in mind, this chapter will succinctly review the following FD-TD modeling validations and examples:

1. Electromagnetic wave scattering, two dimensions
   a. Square metal cylinder, TM polarization
   b. Circular muscle-fat layered cylinder, TE polarization
   c. Homogeneous, anisotropic, square material cylinder
   d. Circular metal cylinder, conformally modeled
   e. Flanged metal open cavity
   f. Relativistically vibrating mirror, oblique incidence
2. Electromagnetic wave scattering, three dimensions
   a. Metal cube, broadside incidence
   b. Flat conducting plate, multiple monostatic looks
   c. T-shaped conducting target, multiple monostatic looks
3. Electromagnetic wave penetration and coupling in 2-D and 3-D
   a. Narrow slots and lapped joints in thick screens
   b. Wires and wire bundles in free space and in a metal cavity
4. Very complex three-dimensional structures
   a. Missile seeker section
   b. Inhomogeneous tissue model of the entire human body
5. Microstrip and microwave circuit models
6. Inverse scattering reconstructions in one and two dimensions

Finally, this chapter will conclude with a discussion of computing resources for FD-TD and the potential impact of massively concurrent machines.

8.2 General Characteristics of FD-TD

As stated, FD-TD is a direct solution of Maxwell's time-dependent curl equations. It employs no potential. Instead, it applies simple, second-order accurate central-difference approximations [1] for the space and time derivatives of the electric and magnetic fields directly to the respective differential operators of the curl equations. This achieves a sampled-data reduction of the continuous electromagnetic field in a volume of space, over a period of time. Space and time discretizations are selected to bound errors in the sampling process, and to insure numerical stability of the algorithm [2]. Electric and magnetic field components are interleaved in space to permit a natural satisfaction of tangential field continuity conditions at media interfaces. Overall, FD-TD is a marching-in-time procedure which simulates the continuous actual waves by sampled-data numerical analogs propagating in a data space stored in a computer. At each time step, the system of equations to update the field components is fully explicit, so that there is no need to set up or solve a set of linear equations, and the required computer storage and running time is proportional to the electrical size of the volume modeled.

Figure 1(a) illustrates the time-domain wave tracking concept of the FD-TD method. A region of space within the dashed lines is selected for field sampling in space and time. At time = 0, it is assumed that all fields within the numerical sampling region are identically zero. An incident plane wave is assumed to enter the sampling region at this point. Propagation of the incident wave is modeled by the commencement of time-stepping, which is simply the implementation of the finite-difference analog of the curl equations. Time-stepping continues as the numerical analog of the incident wave strikes the modeled target embedded within the sampling region. All outgoing scattered wave analogs ideally propagate through the lattice truncation planes with negligible reflection to exit the sampling region. Phenomena such as induction of surface currents, scattering and multiple scattering, penetration through apertures, and cavity excitation are modeled time-step by time-step by the action of the curl equations analog. Self-consistency of these modeled phenomena is generally assured if their spatial and temporal variations are well resolved by the space and time sampling process.

Time-stepping is continued until the desired late-time pulse response or steady-state behavior is observed. An important example of

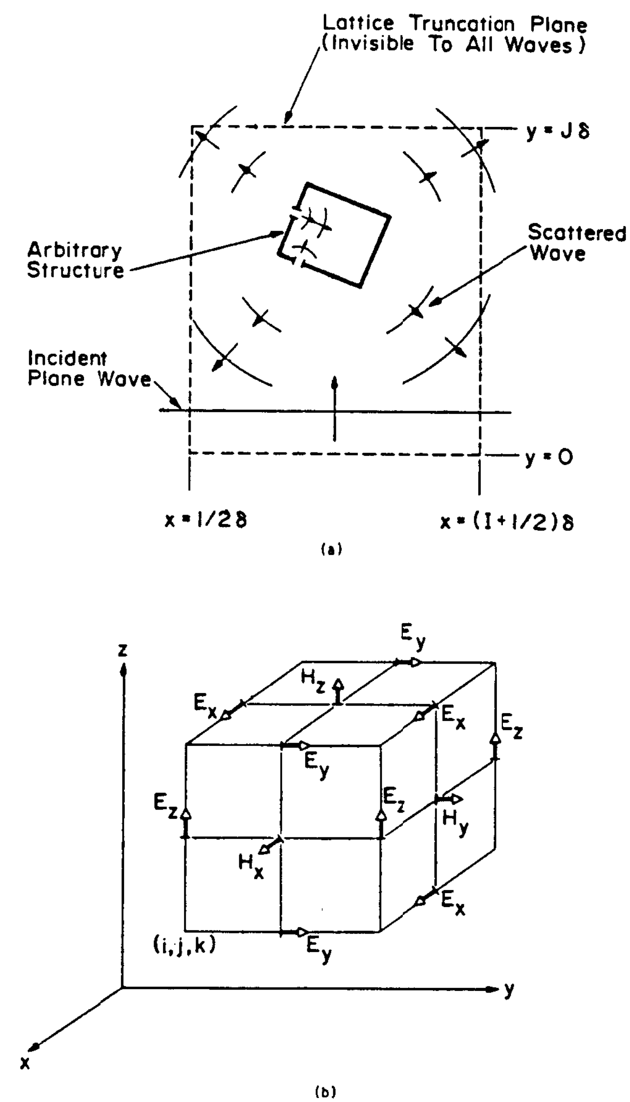

Figure 1 Basic elements of the FD-TD space lattice: (a) Time-domain wave tracking concept; (b) Lattice unit cell in Cartesian coordinates [1].

the latter is the sinusoidal steady state, wherein the incident wave is assumed to have a sinusoidal dependence, and time-stepping is continued until all fields in the sampling region exhibit sinusoidal repetition. This is a consequence of the limiting amplitude principle [3]. Extensive numerical experimentation with FD-TD has shown that the number of complete cycles of the incident wave required to be time-stepped to achieve the sinusoidal steady state is approximately equal to the Q factor of the structure or phenomenon being modeled.

Figure 1(b) illustrates the positions of the electric and magnetic field components about a unit cell of the FD-TD lattice in Cartesian coordinates [1]. Note that each magnetic field vector component is surrounded by four circulating electric field vector components, and vice versa. This arrangement permits not only a centered-difference analog to the space derivatives of the curl equations, but also a natural geometry for implementing the integral form of Faraday's law and Ampere's Law at the space-cell level. This integral interpretation permits a simple but effective modeling of the physics of thin-slot coupling, thin-wire coupling, and smoothly curved target surfaces, as will be seen later.

Figure 2 illustrates how an arbitrary three-dimensional scatterer is embedded in an FD-TD space lattice comprised of the unit cells of Fig. 1(b). Simply, the desired values of electrical permittivity and conductivity are assigned to each electric field component of the lattice. Correspondingly, desired values of magnetic permeability and equivalent conductivity are assigned to each magnetic field component of the lattice. The media parameters are interpreted by the FD-TD program as local coefficients for the time-stepping algorithm. Specification of media properties in this component-by-component manner results in a stepped-edge, or staircase approximation of curved surfaces. Continuity of tangential fields is assured at the interface of dissimilar media with this procedure. There is no need for special field matching at media interface points. Stepped-edge approximation of curved surfaces has been found to be adequate in the FD-TD modeling problems studied in the 1970's and early 1980's, including wave interactions with biological tissues [4], penetration into cavities [5,6], and electromagnetic pulse (EMP) interactions with complex structures [7–9]. However, recent interest in wide dynamic range models of scattering by curved targets has prompted the development of surface-conforming FD-TD approaches which eliminate staircasing. These will be summarized later in this chapter.

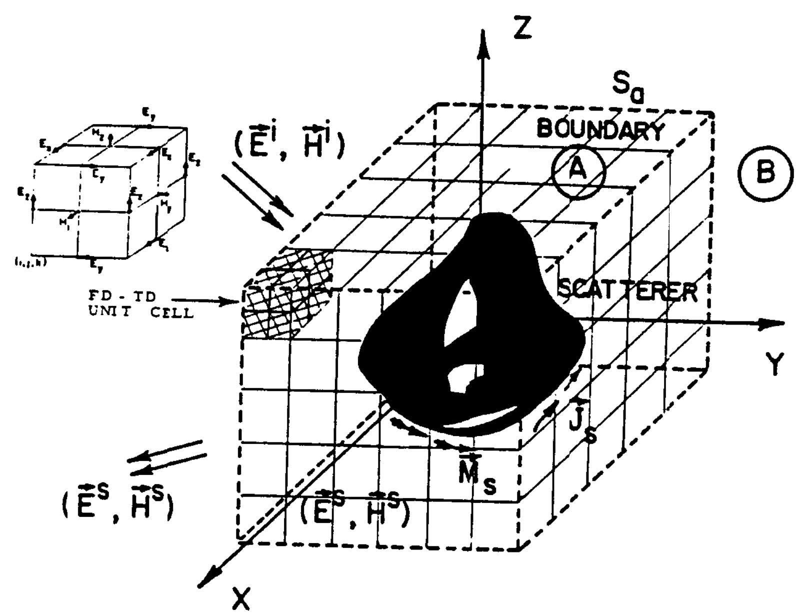

Figure 2 Arbitrary 3-D scatterer embedded in a FD-TD lattice.

8.3 Basic FD-TD Algorithm Details

a. *Maxwell's Curl Equations*

Consider a region of space which is source-free and has constitutive electrical parameters that are independent of time. Then, using the MKS system of units, Maxwell's curl equations are given by

$$\frac{\partial \overline{H}}{\partial t} = -\frac{1}{\mu}\nabla \times \overline{E} - \frac{\rho'}{\mu}\overline{H} \tag{1}$$

$$\frac{\partial \overline{E}}{\partial t} = \frac{1}{\epsilon}\nabla \times \overline{H} - \frac{\sigma}{\epsilon}\overline{E} \tag{2}$$

where $\overline{E}$ is the electric field in volts/meter; $\overline{H}$ is the magnetic field in amperes/meter; ϵ is the electrical permittivity in farads/meter; σ is the electrical conductivity in mhos/meter (siemens/meter); μ is the magnetic permeability in henrys/meter; and ρ' is an equivalent magnetic resistivity in ohms/meter. (The magnetic resistivity term is provided to yield symmetric curl equations, and allow for the possibility of a magnetic field loss mechanism.) Assuming that ϵ, σ, μ, and ρ' are isotropic, the following system of scalar equations is equivalent to Maxwell's curl equations in the rectangular coordinate system (x, y, z)

$$\frac{\partial H_x}{\partial t} = \frac{1}{\mu}\left(\frac{\partial E_y}{\partial z} - \frac{\partial E_z}{\partial y} - \rho' H_x\right) \tag{3a}$$

$$\frac{\partial H_y}{\partial t} = \frac{1}{\mu}\left(\frac{\partial E_z}{\partial x} - \frac{\partial E_x}{\partial z} - \rho' H_y\right) \tag{3b}$$

$$\frac{\partial H_z}{\partial t} = \frac{1}{\mu}\left(\frac{\partial E_x}{\partial y} - \frac{\partial E_y}{\partial x} - \rho' H_z\right) \tag{3c}$$

$$\frac{\partial E_x}{\partial t} = \frac{1}{\epsilon}\left(\frac{\partial H_z}{\partial y} - \frac{\partial H_y}{\partial z} - \sigma E_x\right) \tag{4a}$$

$$\frac{\partial E_y}{\partial t} = \frac{1}{\epsilon}\left(\frac{\partial H_x}{\partial z} - \frac{\partial H_z}{\partial x} - \sigma E_y\right) \tag{4b}$$

$$\frac{\partial E_z}{\partial t} = \frac{1}{\epsilon}\left(\frac{\partial H_y}{\partial x} - \frac{\partial H_x}{\partial y} - \sigma E_z\right) \tag{4c}$$

The system of six coupled partial differential equations of (3) and (4) forms the basis of the FD-TD algorithm for electromagnetic wave interactions with general three-dimensional objects. Before proceeding with the details of the algorithm, it is informative to consider one important simplification of the full three-dimensional case. Namely, if we assume that neither the incident plane wave excitation nor the modeled geometry has any variation in the z-direction (i.e., all partial derivatives with respect to z equal zero), Maxwell's curl equations reduce to two decoupled sets of scalar equations. These decoupled sets, termed the transverse magnetic (TM) mode and the transverse electric (TE) mode, describe two-dimensional wave interactions with objects. The relevant equations for each case follow

TM case (E_z, H_x, and H_y field components only)

$$\frac{\partial H_x}{\partial t} = -\frac{1}{\mu}\left(\frac{\partial E_z}{\partial y} + \rho' H_x\right) \tag{5a}$$

$$\frac{\partial H_y}{\partial t} = \frac{1}{\mu}\left(\frac{\partial E_z}{\partial x} - \rho' H_y\right) \tag{5b}$$

$$\frac{\partial E_z}{\partial t} = \frac{1}{\epsilon}\left(\frac{\partial H_y}{\partial x} - \frac{\partial H_x}{\partial y} - \sigma E_z\right) \tag{5c}$$

TE case (H_z, E_x, and E_y field components only)

$$\frac{\partial E_x}{\partial t} = \frac{1}{\epsilon}\left(\frac{\partial H_z}{\partial y} - \sigma E_x\right) \tag{6a}$$

$$\frac{\partial E_y}{\partial t} = -\frac{1}{\epsilon}\left(\frac{\partial H_z}{\partial x} + \sigma E_y\right) \tag{6b}$$

$$\frac{\partial H_z}{\partial t} = \frac{1}{\mu}\left(\frac{\partial E_x}{\partial y} - \frac{\partial E_y}{\partial x} - \rho' H_z\right) \tag{6c}$$

b. The Yee Algorithm

In 1966, Yee [1] introduced a set of finite-difference equations for the system of (3) and (4). Following Yee's notation, we denote a space point in a rectangular lattice as

$$(i, j, k) = (i\Delta x, j\Delta y, k\Delta z) \tag{7a}$$

and any function of space and time as

$$F^n(i, j, k) = F(i\Delta x, j\Delta y, k\Delta z, n\Delta t) \tag{7b}$$

where $\Delta x, \Delta y$, and Δz are, respectively, the lattice space increments in the x, y, and z coordinate directions; Δt is the time increment; and i, j, k, and n are integers. Yee used centered finite-difference expressions for the space and time derivatives that are both simply programmed and second-order accurate in the space and time increments, respectively:

$$\frac{\partial F^n(i,j,k)}{\partial x} = \frac{F^n(i+\frac{1}{2},j,k) - F^n(i-\frac{1}{2},j,k)}{\Delta x} + O(\Delta x^2) \tag{8a}$$

$$\frac{\partial F^n(i,j,k)}{\partial t} = \frac{F^{n+\frac{1}{2}}(i,j,k) - F^{n-\frac{1}{2}}(i,j,k)}{\Delta t} + O(\Delta t^2) \tag{8b}$$

To achieve the accuracy of (8a), and to realize all of the required space derivatives of the system of (3) and (4), Yee positioned the components of $\overline{E}$ and $\overline{H}$ about a unit cell of the lattice as shown in Fig. 1(b). To achieve the accuracy of (8b), he evaluated $\overline{E}$ and $\overline{H}$ at alternate half time steps. The following are sample finite-difference time-stepping expressions for a magnetic and an electric field component resulting from these assumptions

$$H_x^{n+\frac{1}{2}}(i,j+\tfrac{1}{2},k+\tfrac{1}{2}) = \frac{1-\frac{\rho'(i,j+1/2,k+1/2)\Delta t}{2\mu(i,j+1/2,k+1/2)}}{1+\frac{\rho'(i,j+1/2,k+1/2)\Delta t}{2\mu(i,j+1/2,k+1/2)}}\cdot H_x^{n-\frac{1}{2}}(i,j+\tfrac{1}{2},k+\tfrac{1}{2})$$

$$+\frac{\Delta t}{\mu(i,j+\frac{1}{2},k+\frac{1}{2})}\cdot\frac{1}{1+\frac{\rho'(i,j+1/2,k+1/2)\Delta t}{2\mu(i,j+1/2,k+1/2)}}\cdot \tag{9}$$

$$\left\{\begin{array}{l}[E_y^n(i,j+\frac{1}{2},k+1)-E_y^n(i,j+\frac{1}{2},k)]/\Delta z+\\ {[E_z^n(i,j,k+\frac{1}{2})-E_z^n(i,j+1,k+\frac{1}{2})]/\Delta y}\end{array}\right\}$$

$$E_z^{n+1}(i,j,k+\tfrac{1}{2}) = \frac{1-\frac{\sigma(i,j,k+\frac{1}{2})\Delta t}{2\epsilon(i,j,k+1/2)}}{1+\frac{\sigma(i,j,k+1/2)\Delta t}{2\epsilon(i,j,k+1/2)}}\cdot E_z^n(i,j,k+\tfrac{1}{2})$$

$$+\frac{\Delta t}{\epsilon(i,j,k+\frac{1}{2})}\cdot\frac{1}{1+\frac{\sigma(i,j,k+1/2)\Delta t}{2\epsilon(i,j,k+1/2)}}\cdot \tag{10}$$

$$\left\{\begin{array}{l}[H_y^{n+\frac{1}{2}}(i+\frac{1}{2},j,k+\frac{1}{2})-H_y^{n+\frac{1}{2}}(i-\frac{1}{2},j,k+\frac{1}{2})]/\Delta x+\\ {[H_x^{n+\frac{1}{2}}(i,j-\frac{1}{2},k+\frac{1}{2})-H_x^{n+\frac{1}{2}}(i,j+\frac{1}{2},k+\frac{1}{2})]/\Delta y}\end{array}\right\}$$

With the system of finite-difference equations represented by (9) and (10), the new value of a field vector component at any lattice point depends only on its previous value and on the previous values of the

components of the other field vector at adjacent points. Therefore, at any given time step, the computation of a field vector can proceed either one point at a time; or, if p parallel processors are employed concurrently, p points at a time.

c. *Numerical Stability*

To insure the stability of the time-stepping algorithm exemplified by (9) and (10), Δt is chosen to satisfy the inequality [2,10]

$$\Delta t \leq \frac{1}{c_{\max}\left\{\frac{1}{\Delta x^2}+\frac{1}{\Delta y^2}+\frac{1}{\Delta z^2}\right\}^{\frac{1}{2}}} \tag{11}$$

where c_{max} is the maximum electromagnetic wave phase velocity within the media being modeled. Note that the corresponding numerical stability criterion set forth in Eqs. (7) and (8) of Reference [1] is incorrect [2]. For the TM and TE two-dimensional modeling cases, it can be shown [10] that the modified time-step limit for numerical stability is obtained from (11) simply by setting $\Delta z = \infty$.

d. *Numerical Dispersion*

The numerical algorithm for Maxwell's curl equations represented by (9) and (10) causes dispersion of the simulated wave modes in the computational lattice. That is, the phase velocity of numerical modes in the FD-TD lattice can vary with modal wavelength, direction of propagation, and lattice discretization. This numerical dispersion can lead to non-physical results such as pulse distortion, artificial anisotropy, and pseudo-refraction. Numerical dispersion is a factor in FD-TD modeling that must be accounted to understand the operation of the algorithm and its accuracy limits.

Following the analysis in [10], it can be shown that the numerical dispersion relation for the three-dimensional case represented by (9) and (10) is given by

$$\left(\frac{1}{c\Delta t}\right)^2\sin^2\left(\frac{\omega\Delta t}{2}\right) = \frac{1}{\Delta x^2}\sin^2\left(\frac{k_x\Delta x}{2}\right)+\frac{1}{\Delta y^2}\sin^2\left(\frac{k_y\Delta y}{2}\right)+\frac{1}{\Delta z^2}\sin^2\left(\frac{k_z\Delta z}{2}\right) \tag{12}$$

where k_x, k_y, and k_z are, respectively, the x, y, and z components of the wavevector; ω is the wave angular frequency; and c is the speed of light in the homogeneous material being modeled.

In contrast to the numerical dispersion relation, the analytical dispersion relation for a plane wave in a continuous, lossless medium is just

$$\omega^2/c^2 = k_x^2 + k_y^2 + k_z^2 \qquad (13)$$

for the three-dimensional case. Although, at first glance, (12) bears little resemblance to the ideal case of (13), we can easily show that (12) reduces to (13) in the limit as $\Delta t, \Delta x, \Delta y$, and Δx all go to zero. Qualitatively, this suggests that numerical dispersion can be reduced to any degree that is desired if we only use a fine-enough FD-TD gridding.

To quantitatively illustrate the dependence of numerical dispersion upon FD-TD grid discretization, we shall take as an example the two-dimensional TM case ($\Delta z = \infty$), assuming for simplicity square unit cells ($\Delta x = \Delta y = \delta$) and wave propagation at an angle α with respect to the positive x-axis ($k_x = k\cos\alpha$; $k_y = \sin\alpha$). Then, dispersion relation (12) simplifies to

$$\left(\frac{\delta}{c\Delta t}\right)^2 \sin^2\left(\frac{\omega\Delta t}{2}\right) = \sin^2\left(\frac{k\delta\cos\alpha}{2}\right) + \sin^2\left(\frac{k\delta\sin\alpha}{2}\right) \qquad (14)$$

(14) can be conveniently solved for the wavevector magnitude, k, by applying Newton's method. This process is especially convenient if δ is normalized to the free-space wavelength.

Figure 3a provides results using this procedure which illustrate the variation of numerical phase velocity with wave propagation angle in the FD-TD grid [10]. Three different grid resolutions of the propagating wave are examined: coarse ($\lambda_0/5$); normal ($\lambda_0/10$); and fine ($\lambda_0/20$). For each resolution, the relation $c\Delta t = \delta/2$ was maintained. This relation is commonly used in two- and three-dimensional FD-TD codes to satisfy the numerical stability criterion of (11) with ample safety margin. From Fig. 3a, it is seen that the numerical phase velocity is maximum at 45° (oblique incidence), and minimum at 0° and 90° (incidence along either Cartesian grid axis) for all grid resolutions. This represents a numerical anisotropy that is inherent in the Yee algorithm. However, the velocity error relative to the ideal case diminishes by approximately a 4:1 factor each time that the grid cell size is halved,

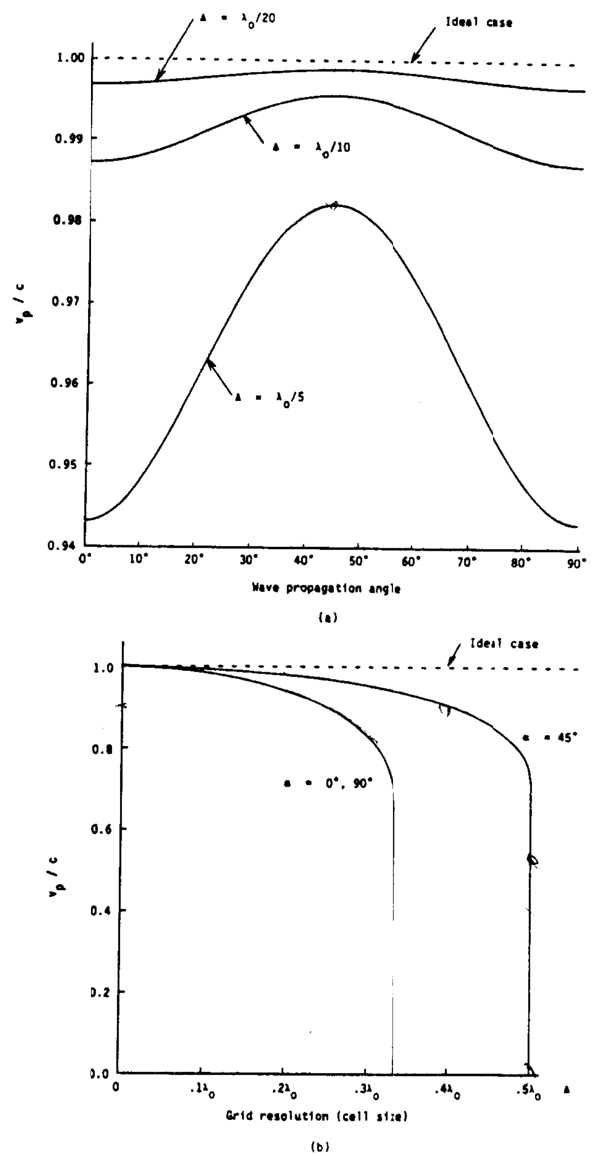

Figure 3 Variation of FD-TD numerical wave phase velocity (dispersion): (a) with wave propagation angle in the grid for three different grid discretizations; (b) with grid resolution for three different wave propagation angles [10].

so that the worst-case velocity error for the normal resolution case is only −1.3%, and only −0.31% for the fine resolution case.

Figure 3(b) graphs the variation of numerical phase velocity with grid resolution at the fixed incidence angles, 45° and 0°(90°). Again, the relation $c\Delta t = \delta/2$ was maintained for each resolution. Here, it is seen that the numerical phase velocity at each angle of incidence diminishes as the propagating wave is more coarsely resolved, eventually reaching a sharp threshold where the numerical phase velocity goes to zero and the wave can no longer propagate in the FD-TD grid. This represents a numerical low-pass filtering effect that is inherent in the Yee algorithm, wherein the wavelength of propagating numerical modes has a lower bound of 2 to 3 space cells, depending upon the propagation direction. As a result, FD-TD modeling of pulses having finite duration (and thus, infinite bandwidth) can result in progressive pulse distortion as higher spatial frequency components propagate more slowly than lower spatial frequency components, and very high spatial frequency components with wavelengths less than 2 to 3 cells are rejected. This numerical dispersion causes broadening of finite-duration pulses, and leaves a residue of high-frequency ringing on the trailing edges due to the relatively slowly propagating high-frequency components. From Figs. 3(a) and 3(b), we see that pulse distortion can be bounded by obtaining the Fourier spatial frequency spectrum of the desired pulse, and selecting a grid cell size so that the principal spectral components are resolved with at least 10 cells per wavelength. This would limit the spread of numerical phase velocities of the principal spectral components to less than 1%, regardless of wave propagation angle in the grid.

In addition to numerical phase velocity anisotropy and pulse distortion effects, numerical dispersion can lead to pseudo-refraction of propagating modes if the grid cell size is a function of position in the grid. Such variable-cell gridding would also vary the grid resolution of propagating numerical modes, and thereby perturb the modal phase velocity distribution. This would lead to non-physical reflection and refraction of numerical modes at interfaces of grid regions having different cell sizes (even if these interfaces were located in free space), just as physical waves undergo reflection and refraction at interfaces of dielectric media having different indices of refraction. The degree of non-physical refraction is dependent upon the magnitude and abruptness of the change of the modal phase velocity distribution, and can be estimated by using conventional theory for wave refraction at dielectric

interfaces.

We have stated that, in the limit of infinitesimal Δt and δ, (12) reduces to (13), the ideal dispersion case. This reduction also occurs if Δt, δ, and the direction of propagation are suitably chosen. For example, in a three-dimensional cubic lattice, reduction to the ideal dispersion case can be demonstrated for wave propagation along a lattice diagonal ($k_x = k_y = k_z = k/\sqrt{3}$) and $\Delta t = \delta/(c\sqrt{3})$ (exactly the limit set by numerical stability). Similarly, in a two-dimensional square grid, the ideal dispersion case can be demonstrated for wave propagation along a grid diagonal ($k_x = k_y = k/\sqrt{2}$) and $\Delta t = \delta/(c\sqrt{2})$ (again the limit set by numerical stability). Finally, in one dimension, the ideal case is obtained for $\Delta t = \delta/c$ (again the limit set by numerical stability) for all propagating modes.

e. *Lattice Zoning and Plane Wave Source Condition*

The numerical algorithm for Maxwell's curl equations defined by the finite-difference system reviewed above has a linear dependence upon the components of the electromagnetic field vectors. Therefore, this system can be applied with equal validity to either the incident-field vector components, the scattered-field vector components, or the total-field vector components (the sum of incident plus scattered). Present FD-TD codes utilize this property to zone the numerical space lattice into two distinct regions, as shown in Fig. 4(a), separated by a rectangular virtual surface which serves to connect the fields in each region [11,12].

Region 1, the inner region of the FD-TD lattice, is denoted as the total- field region. Here, it is assumed that the finite-difference system for the curl equations operates on total-field vector components. The interacting structure of interest is embedded within this region.

Region 2, the outer region of the FD-TD lattice, is denoted as the scattered-field region. Here, it is assumed that the finite-difference system for the curl equations operates only on scattered-field vector components. This implies that there is no incident wave in Region 2. The outer lattice planes bounding Region 2, called the lattice truncation planes, serve to implement the free-space radiation condition (discussed in the next section) which simulates the field sampling space extending to infinity.

The total-field/scattered-field lattice zoning illustrated in Fig. 4(a) provides a number of key features which enhance the computational

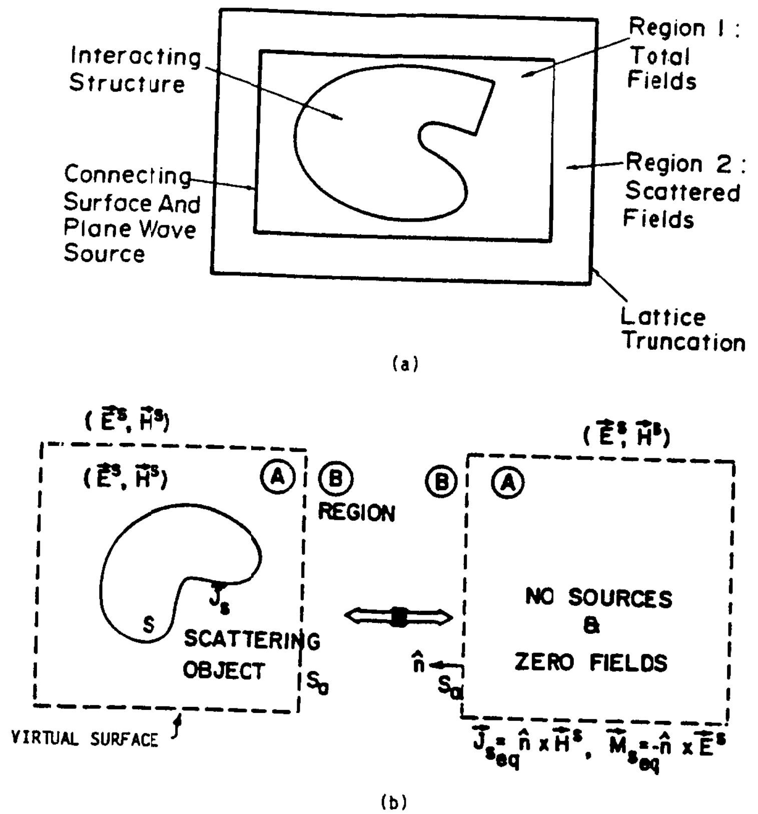

Figure 4 **Zoning of the FD-TD lattice: (a) Total field and scattered field regions [11,12]; (b) Near-to-far field integration surface located in the scattered field region [12].**

flexibility and dynamic range of the FD-TD method:

Arbitrary incident wave. The connecting condition provided at the interface of the inner and outer regions, which assures consistency of the numerical space derivative operations across the interface, simultaneously generates an arbitrary incident plane wave in Region 1 having a user-specified time waveform, angle of incidence, and angle of polarization. This connecting condition, discussed in detail in [10], almost completely confines the incident wave to Region 1 and yet is transparent to outgoing scattered wave modes which are free to enter Region 2.

Simple programming of inhomogeneous structures. The required continuity of total tangential E and H fields across the interface of dissimilar media is automatically provided by the original Yee algorithm if the media are located in a zone (such as Region 1) where total fields are time-marched. This avoids the problems inherent in a pure scattered-field code where enforcement of the continuity of total tangential fields is a separate process requiring the incident field to be computed at all interfaces of dissimilar media, and then added to the values of the time-marched scattered fields at the interfaces. Clearly, computation of the incident field at numerous points along possibly complex, structure-specific loci is likely to be much more involved than computation of the incident field only along the simple connecting surface between Regions 1 and 2 (needed to implement the total-field/scattered-field zoning). The latter surface has a fixed locus that is independent of the shape or complexity of the interaction structure that is embedded in Region 1.

Wide computational dynamic range. Low levels of the total field in deep shadow regions or cavities of the interaction structure are computed directly by time-marching total fields in Region 1. In a pure scattered-field code, however, the low levels of total field are obtained by computing the incident field at each desired point, and then adding to the values of the time-marched scattered fields. Thus, it is seen that a pure scattered-field code relies upon near cancellation of the incident and scattered field components of the total field to obtain accurate results in deep shadow regions and cavities. An undesirable hallmark of this cancellation is contamination of the resultant low total-field level by subtraction noise, wherein slight percentage errors in calculating the scattered fields result in possibly very large percentage errors in the residual total fields. By time-marching total fields directly, the zoned FD-TD code avoids subtraction noise in Region 1 and achieves a computational dynamic range more than 30 dB greater than that for a pure scattered-field code.

Far-field response. The provision of a well-defined scattered-field region in the FD-TD lattice permits the near-to-far field transformation illustrated in Fig. 4(b) [12]. The dashed virtual surface shown in Fig. 4(b) can be located along convenient lattice planes in the scattered field region of Fig. 4(a). Tangential scattered E and H fields computed via FD-TD at this virtual surface can then be weighted by the free space Green's function and then integrated (summed) to provide th far-field response and radar cross section (full bistatic response for the assumed illumination angle) [12–14]. The near-field integration surface has a fixed rectangular shape, and thus is independent of the shape or composition of the enclosed structure being modeled.

8.4 Contour Path Interpretation

a. *Usefulness*

The Yee algorithm for FD-TD was originally interpreted as a direct approximation of the pointwise derivatives of Maxwell's time-dependent curl equations by using numerical central differences [1]. Although this interpretation is useful for understanding how FD-TD models wave propagation away from material surfaces, it sheds little light on what algorithm modifications are needed to properly model the physics of fine geometrical features such as wires, slots, and curved surfaces requiring sub-cell spatial resolution. Modeling of such features has become increasingly important as confidence in the basic predictive powers of FD-TD has grown.

Recent work has indicated that extension of FD-TD modeling to wires, slots, and curved surfaces can be achieved by departing from Yee's original pointwise derivative interpretation. As shown in Fig. 5, the new idea involves starting with a more macroscopic (but still local) combined-field description based upon Ampere's Law and Faraday's Law in *integral* form, implemented on an array of electrically small, spatially orthogonal contours. These contours mesh (intersect) in the manner of links in a chain, providing a geometrical interpretation of the coupling of Ampere's Law and Faraday's Law. This meshing results in the filling of the FD-TD modeled space by a three-dimensional chain-link array of intersecting, orthogonal contours. The presence of wires, slots, and curved surfaces can be accounted by incorporating appropriate field behavior into the contour and surface integrals implementing Ampere's Law and Faraday's Law at selected meshes, and by deforming contour paths as required to conform with surface curvature.

b. *Equivalence to the Yee Algorithm in Free Space*

We shall first demonstrate the equivalence of the Yee and contour path interpretations for the free-space case [15]. For simplicity, FD-TD expressions will be developed for only one field component in Fig. 5(a)

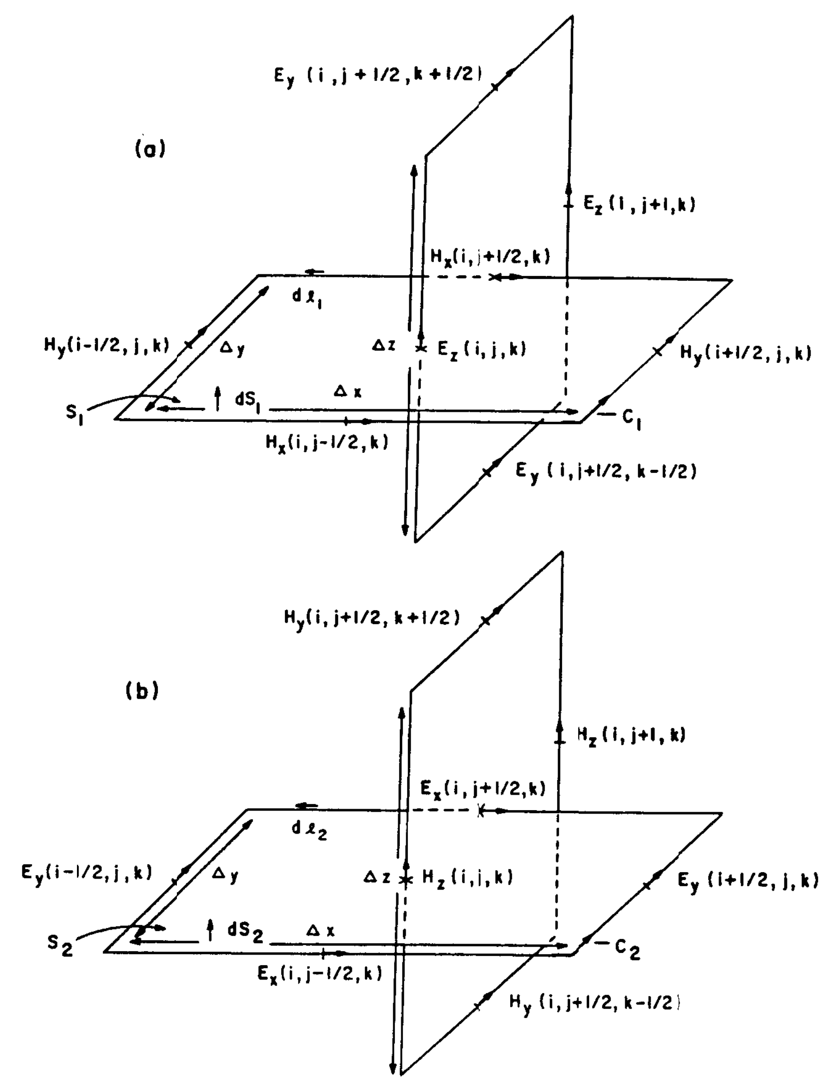

Figure 5 Examples of spatially orthogonal contours in free space: (a) Ampere's Law for E_z; (b) Faraday's Law for H_z [15].

and one field component in Fig. 5(b); extension to all of the rest will be seen to be straightforward.

Applying Ampere's Law along C_1 in Fig. 5(a), and assuming that the field value at a midpoint of one side of the contour equals the average value of that field component along that side, we obtain

$$\frac{\partial}{\partial t}\int_{S_1} \overline{D}\cdot d\overline{S}_1 = \oint_{C_1} \overline{H}\cdot \overline{dl}_1 \tag{15a}$$

$$\frac{\partial}{\partial t}\int_{S_1} \epsilon_0 E_z(i,j,k)dS_1 \simeq H_x(i,j-\tfrac{1}{2},k)\Delta x + H_y(i+\tfrac{1}{2},j,k)\Delta y - H_x(i,j+\tfrac{1}{2},k)\Delta x - H_y(i-\tfrac{1}{2},j,k)\Delta y \tag{15b}$$

Now, further assuming that $E_z(i,j,k)$ equals the average value of E_z over the surface, S_1; that $\Delta x = \Delta y = \delta$; and that the time derivative can be numerically realized by using a central-difference expression, (15b) reduces to

$$\epsilon_0\delta^2\cdot\left[\frac{E_z^{n+1}(i,j,k) - E_z^{n}(i,j,k)}{\Delta t}\right] = \left[\begin{array}{l} H_x^{n+\frac{1}{2}}(i,j-\frac{1}{2},k) - H_x^{n+\frac{1}{2}}(i,j+\frac{1}{2},k) + \\ H_y^{n+\frac{1}{2}}(i+\frac{1}{2},j,k) - H_y^{n+\frac{1}{2}}(i-\frac{1}{2},j,k) \end{array}\right]\cdot\delta \tag{15c}$$

where the superscripts indicate field values at time steps $n, n+\frac{1}{2}$, and $n+1$. Isolation of $E_z^{n+1}(i,j,k)$ on the left hand side then yields exactly the Yee time-stepping expression for E_z for the free-space case that was obtained directly from implementing the curl $\overline{H}$ equation.

In an analogous manner, we can apply Faraday's Law along contour C_2 in Fig. 5(b) to obtain:

$$\frac{\partial}{\partial t}\int_{S_2} \overline{B}\cdot d\overline{S}_2 = -\oint_{C_2} \overline{E}\cdot \overline{dl}_2 \tag{16a}$$

$$\frac{\partial}{\partial t}\int_{S_2} \mu_0 H_z(i,j,k)dS_2 \simeq -E_x(i,j-\tfrac{1}{2},k)\Delta x - E_y(i+\tfrac{1}{2},j,k)\Delta y + E_x(i,j+\tfrac{1}{2},k)\Delta x + E_y(i-\tfrac{1}{2},j,k)\Delta y \tag{16b}$$

$$\mu_0\delta^2\cdot\left[\frac{H_z^{n+\frac{1}{2}}(i,j,k) - H_z^{n-\frac{1}{2}}(i,j,k)}{\Delta t}\right] = \left[\begin{array}{l} E_x^{n}(i,j+\frac{1}{2},k) - E_x^{n}(i,j-\frac{1}{2},k) + \\ E_y(i-\frac{1}{2},j,k) - E_y(i+\frac{1}{2},j,k) \end{array}\right]\cdot\delta \tag{16c}$$

Isolation of $H_z^{n+\frac{1}{2}}(i,j,k)$ on the left hand side yields exactly the Yee time-stepping expression for H_z, for the free-space case, that was obtained directly from implementing the curl $\overline{E}$ equation with finite differences.

c. *Example 1: Application to the Thin Slot*

To illustrate how the contour path interpretation provides the basis for FD-TD modeling of fine geometrical features requiring sub-cell spatial resolution, we first consider the thin slot in a planar, perfectly-conducting screen of finite size and thickness subjected to TE illumination [15]. Figure 6 illustrates the canonical slot geometry studied here, and the Faraday's Law contour paths, C_1, C_2, and C_3, used to derive special FD-TD algorithms for the longitudinal magnetic field components, H_z, located immediately adjacent to the screen.

The following briefly summarizes the assumptions concerning the near-field physics that are incorporated into the Faraday's Law models of Fig. 6. First, for contour C_1 (away from the slot), field components, H_z and E_y, are assumed to have no variation in the y direction (perpendicular to the screen). Evaluated at the x midpoint of contour C_1, H_z, and E_x are assumed to represent the average values of their respective fields over the full x interval. At contour C_2 (at the opening of the slot), H_z is assumed to represent the average value of the magnetic field over the entirety of the free-space part of S_2. Here, E_y is again assumed to have no variation in the y direction, and E_x is again assumed to represent the average value over the full x interval. At contour C_3 (within the slot), H_z is assumed to represent the average value of the magnetic field over the full y interval, and H_z and E_x are assumed to have no variation in the x direction (across the slot gap). Finally, for C_1, C_2, and C_3, the portions of the contours located within the conducting screen are assumed to have zero electric and magnetic

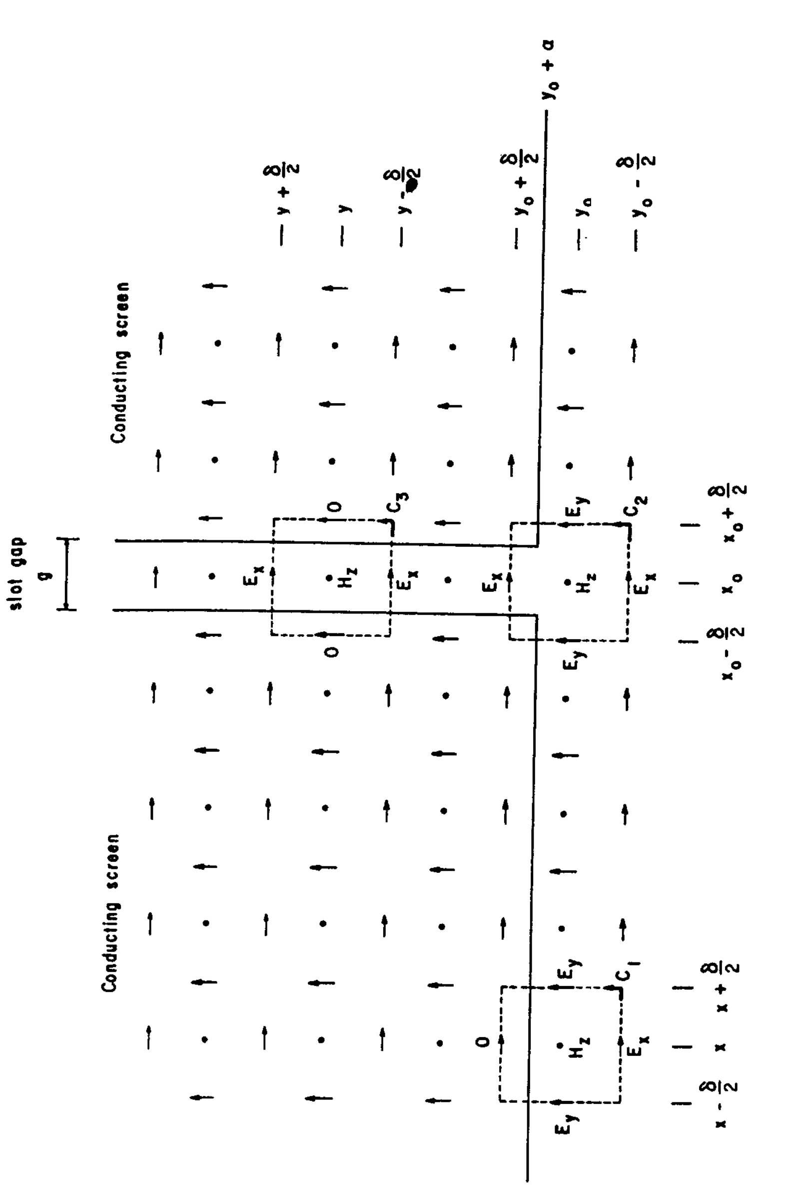

Figure 6 Faraday's Law contour paths for a 2-D planar conducting screen with a thin slot (TE case) [15].

fields.

After applying Faraday's Law of (16a) for the three contours subject to the above assumptions, the following special FD-TD time-stepping relations are obtained for the H_z components immediately adjacent to the screen

Away from the slot (contour C_1)

$$\frac{H_z^{n+\frac{1}{2}}(x,y_0) - H_z^{n-\frac{1}{2}}(x,y_0)}{\Delta t} \simeq \frac{[E_y^n(x-\frac{\delta}{2},y_0) - E_y^n(x+\frac{\delta}{2},y_0)]\cdot(\frac{\delta}{2}+\alpha) - E_x^n(x,y_0-\frac{\delta}{2})\cdot\delta}{\mu_0\delta(\frac{\delta}{2}+\alpha)} \tag{17a}$$

At the opening (aperture) of the slot (contour C_2)

$$\frac{H_z^{n+\frac{1}{2}}(x_0,y_0) - H_z^{n-\frac{1}{2}}(x_0,y_0)}{\Delta t} \simeq \frac{\begin{pmatrix} E_x^n(x_0,y_0+\frac{\delta}{2})\cdot g - E_x^n(x_0,y_0-\frac{\delta}{2})\cdot\delta + \\ [E_y^n(x_0-\frac{\delta}{2},y_0) - E_y^n(x_0+\frac{\delta}{2},y_0)]\cdot(\frac{\delta}{2}+\alpha) \end{pmatrix}}{\mu_0\cdot\left[\delta(\frac{\delta}{2}+\alpha)+g(\frac{\delta}{2}-\alpha)\right]} \tag{17b}$$

Within the slot (contour C_3)

$$\frac{H_z^{n+\frac{1}{2}}(x_0,y) - H_z^{n-\frac{1}{2}}(x_0,y)}{\Delta t} \simeq \frac{E_x^n(x_0,y+\frac{\delta}{2})\cdot g - E_x^n(x_0,y-\frac{\delta}{2})\cdot g}{\mu_0 g\delta} \tag{17c}$$

In (17c), we note that the slot gap distance, g, cancels on the right hand side, reducing the time-stepping relation for H_z in the slot to that of a one-dimensional wave ($\pm y$-directed) in free space. For completeness, we also note that no magnetic or electric field components in the FD-TD space grid, other than the H_z components immediately adjacent to the screen, require modified time-stepping relations.

The accuracy of this contour integral model implemented on a coarse FD-TD grid (having 1/10 wavelength cell size) will be examined in section 8.8a for two cases: (1) a straight slot in a thick conducting screen; and (2) a U-shaped lapped joint in a thick conducting screen, exhibiting resonant transmission and gap-field phenomena. Excellent correspondence with high-resolution method of moments and FD-TD numerical benchmarks will be shown.

d. *Example 2: Application to the Thin Wire*

A second illustration of how the contour path interpretation permits incorporation of near-field physics (yielding special-purpose time-stepping expressions that were *not* obvious from the previous pure finite-difference perspective) is provided by considering coupling to a sub-cell diameter wire [16]. Figure 7 illustrates the Faraday's Law contour path used to derive the special FD-TD algorithm for the circumferential magnetic fields immediately adjacent to the wire. Although only H_y is shown, the analysis is easily generalized for the other adjacent, looping magnetic field components.

The following briefly summarizes the assumptions concerning the near-field physics that are incorporated into the Faraday's Law model. First, the near scattered circumferential magnetic field components and the near scattered radial electric field components are assumed to vary as $1/r$ near the wire, where r is the distance from the wire center. With r constrained to be less than 0.1 wavelength at any point in C (by FD-TD spatial resolution requirements), the $1/r$ singularity behavior of the scattered H_y and E_x fields is assumed to dominate the respective incident fields, so that the total H_y and E_x fields also take on the $1/r$ singularity. Finally, the near total H_y and the near total E_z fields, evaluated at the z midpoint of the contour, are assumed to represent the average values of their respective fields over the full z interval. These assumptions can be concisely summarized by the following expressions, assumed to apply on and within contour C of Fig. 7

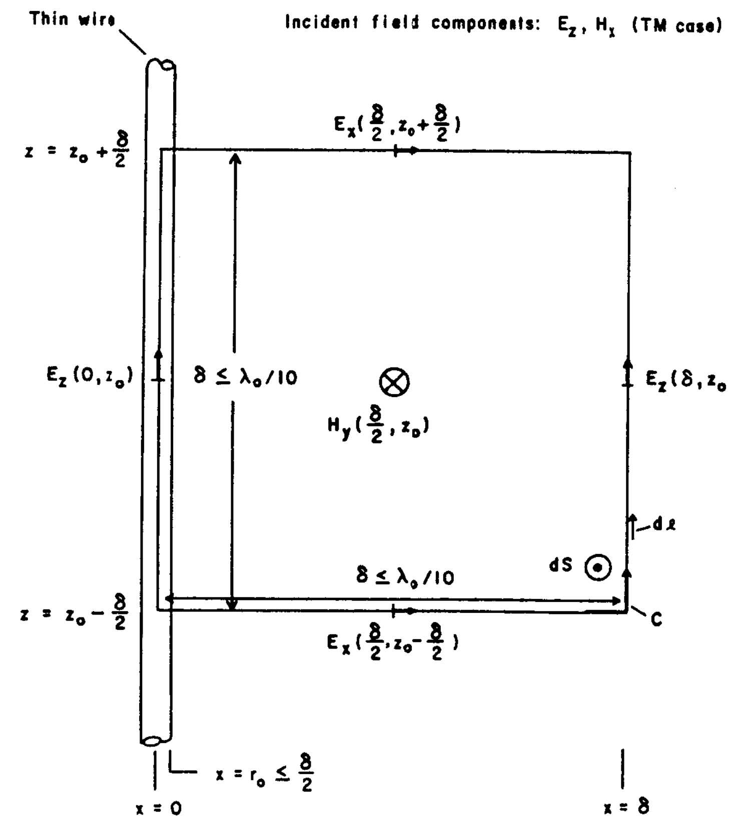

Figure 7 **Faraday's Law contour path for thin-wire model [16'**

$$H_y(x,z) \simeq H_y(\frac{\delta}{2}, z_0) \cdot \frac{(\frac{\delta}{2})}{x} \cdot [1 + c_1 \cdot (z - z_0)]$$

$$E_x(x, z_0 \pm \frac{\delta}{2}) \simeq E_x(\frac{\delta}{2}, z_0 \pm \frac{\delta}{2}) \cdot \frac{(\frac{\delta}{2})}{x}$$

$$E_z(0,z) = 0$$

$$E_z(\delta, z) \simeq E_z(\delta, z_0) \cdot [1 + c_2 \cdot (z - z_0)] \qquad \text{(18d}$$

where c_1 and c_2 are arbitrary constants that need not be known.

Using the field expressions of (18a)–(18d), we can now apply Faraday's Law of (16a) along contour C. We find that the $1/x$ variations in H_y and E_x yield natural logarithms. Further, the linear, odd symmetry variation in z assumed for H_y and E_z integrates out. This yields the following expression

$$\frac{H_y^{n+\frac{1}{2}}(\frac{\delta}{2}, z_0) - H_y^{n-\frac{1}{2}}(\frac{\delta}{2}, z_0)}{\Delta t} \simeq$$

$$\frac{[E_x^n(\frac{\delta}{2}, z_0 - \frac{\delta}{2}) - E_x^n(\frac{\delta}{2}, z_0 + \frac{\delta}{2})] \cdot \frac{1}{2} \ln\left(\frac{\delta}{r_0}\right) + E_z^n(\delta, z_0)}{\mu_0 \frac{\delta}{2} \ln\left(\frac{\delta}{r_0}\right)} \tag{19}$$

where r_0 (assumed to be less than 0.5 δ) is the wire radius. Isolation of $H_y^{n+\frac{1}{2}}(\frac{\delta}{2}, z_0)$ on the left hand side of (19) yields the required modified time-stepping relation. As stated, the analysis is easily generalized to obtain similar time-stepping relations for the other circumferential magnetic field components immediately adjacent to the wire. It should be noted that *no* other magnetic or electric field components in the FD-TD space lattice require modified time-stepping relations. All other field components are time-stepped by using the ordinary free-space Yee algorithm of section 8.3.

The accuracy of this contour integral model implemented on a coarse FD-TD grid will be examined in section 8.8b for four cases: (1) TM illumination of an infinitely long wire over a very wide range of wire radius; (2) broadside illumination of a two-wavelength long (antiresonant) dipole; (3) broadside illumination of a four-wire bundle where the entire bundle diameter is less than one space cell; and (4) coupling to a single wire and a wire-pair within an aperture-perforated metal cavity exhibiting a moderate-Q (30 to 80) resonant response. Excellent correspondence with either method of moments numerical results or experimental data will be shown.

8.5 Radiation Boundary Conditions

A basic consideration with the FD-TD approach to solve electromagnetic field problems is that most such problems are usually considered to be "open" problems where the domain of the computed field is ideally unbounded. Clearly, no computer can store an unlimited

amount of data, and therefore, the field computation zone must b limited in size. The computation zone must be large enough to enclos the structure of interest, and a suitable boundary condition on th outer perimeter of the computation zone must be used to simulate th extension of the computation zone to infinity. This boundary conditio suppresses spurious reflections of outward-propagating wave analogs t some acceptable level, permitting the FD-TD solution to remain vali for all time steps (especially after spurious reflected wave analogs re turn to the vicinity of the modeled structure). Outer lattice boundar conditions of this type have been called either radiation boundary con ditions (RBC's), absorbing boundary conditions (ABC's), or lattic truncation conditions.

The radiation condition cannot be directly obtained from the nu merical algorithms for Maxwell's curl equations defined by the finite difference systems reviewed in section 8.3. Principally, this is becaus these systems employ a central-difference scheme which requires knowl edge of the field one-half space cell to each side of an observation point Central differences cannot be implemented at the outermost lattic plane since, by definition, there is no information concerning the field at points one-half space cell outside of the outermost lattice plane.

This section will develop the theory and numerical implementatio of a very useful radiation condition in Cartesian coordinates. Th radiation condition is appropriate for effectively truncating a two- o three-dimensional FD-TD space lattice with an overall level of spuriou reflections of 1%–5% for outer lattice planes located 10-20 space cell from a target surface. The radiation condition will be derived using recent theoretical approach, wave equation factoring. An approach t improvement of the currently used radiation boundary condition wil also be summarized.

a. *One-Way Wave Equations*

A partial differential equation which permits wave propagatio only in certain directions is called a "one-way wave equation." Figur 8 shows a finite, two-dimensional Cartesian domain, Ω, on which th time-dependent wave equation is to be simulated. In the interior o Ω, a numerical scheme (such as the algorithms of section 8.3) whic models wave propagation in all directions is applied. On $\partial\Omega$, the oute boundary of Ω, only numerical wave motion that is outward from Ω i permitted. The boundary must permit outward propagating numerica

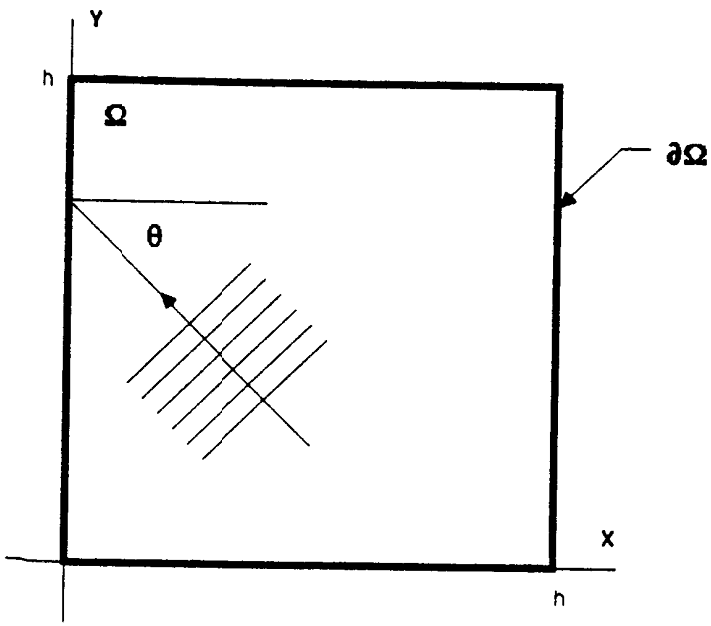

Figure 8 Numerical plane-wave analog incident upon left grid boundary of a 2-D Cartesian computational domain.

wave analogs to exit Ω just as if the simulation were performed on a computational domain of infinite extent. A scheme which enacts a one-way wave equation on ∂Ω for this purpose is called a radiation boundary condition (RBC).

b. *Derivation by Wave Equation Factoring*

The derivation of an RBC whose purpose is to absorb numerical waves incident upon the outer boundary of a finite-difference grid can be explained in terms of operator factoring. For example, consider the two-dimensional wave equation in Cartesian coordinates

$$U_{xx} + U_{yy} - \frac{1}{c^2}U_{tt} = 0 \tag{20}$$

where U is a scalar field component; the subscripts xx, yy, and tt denote second partial derivatives with respect to x, y, and t, respectively; and

c is the wave phase velocity. The partial differential operator here is

$$L \equiv D_x^2 + D_y^2 - \frac{1}{c^2}D_t^2 \quad (21a)$$

which uses the notation

$$D_x^2 \equiv \frac{\partial^2}{\partial x^2};\ D_y^2 \equiv \frac{\partial^2}{\partial y^2};\ D_t^2 \equiv \frac{\partial^2}{\partial t^2} \quad (21b)$$

The wave equation is then compactly written as

$$LU = 0 \quad (22)$$

The wave operator, L, can be factored in the following manner:

$$LU = L^+L^-U = 0 \quad (23a)$$

where L^- is defined as

$$L^- \equiv D_x - \frac{D_t}{c}\sqrt{1 - S^2} \quad (23b)$$

with

$$S = \frac{D_y}{(D_t/c)} \quad (23c)$$

The operator, L^+, is similarly defined except for a " + " sign befor the radical.

Engquist and Majda [17] showed that at a grid boundary, say a $x = 0$, the application of L^- to the wave function, U, will exactl absorb a plane wave propagating toward the boundary at an arbitrar angle, θ. Thus,

$$L^-U = 0 \quad (24)$$

applied at $x = 0$ functions as an exact analytical RBC which absorl wave motion from the interior of the spatial domain, Ω. The operato L^+, performs the same function for a plane wave propagating at a arbitrary angle toward the other x boundary in Fig. 8 at $x = h$. Th presence of the radical in (23b) classifies L^- as a pseudo-differenti operator that is non-local in both the space and time variables. This an undesirable characteristic in that it prohibits the direct numeric implementation of (24) as an RBC.

Approximations of the radical in (23b) produce RBC's that can be implemented numerically and are useful in FD-TD simulations. The numerical implementation of an RBC is not exact in that a small amount of reflection does develop as numerical waves pass through the grid boundary. However, it is possible to design an RBC which minimizes the reflection over a range of incident angles. The Mur RBC, used in current FD-TD electromagnetic wave codes, is simply a two-term Taylor series approximation to the radical in (23b), given by [11]

$$\sqrt{1-S^2} \simeq 1 - \frac{1}{2}S^2 \tag{25a}$$

Substituting (25a) into (24), we obtain

$$\left(D_x - \frac{D_t}{c} + \frac{cD_y^2}{2D_t}\right)U = 0 \tag{25b}$$

Multiplying (25b) through by D_t, and identifying the differential operators as partial derivatives, we obtain the following approximate, analytical RBC which can be numerically implemented at the $x = 0$ grid boundary

$$U_{xt} - \frac{1}{c}U_{tt} + \frac{c}{2}U_{yy} = 0 \tag{26}$$

Equation (26) is a very good approximation to the exact RBC of (24) for relatively small values of $S = cD_y/D_t$ which satisfy the Taylor series approximation of (25a). This is equivalent to saying that (26) presents a nearly reflectionless grid truncation for numerical plane wave modes which strike the $x = 0$ grid boundary at small values of the incident angle, θ. Analogous approximate, analytical RBC's can be derived for the other grid boundaries

$$U_{xt} + \frac{1}{c}U_{tt} - \frac{c}{2}U_{yy} = 0, \quad x = h \text{ boundary} \tag{27a}$$

$$U_{yt} - \frac{1}{c}U_{tt} + \frac{c}{2}U_{xx} = 0, \quad y = 0 \text{ boundary} \tag{27b}$$

$$U_{yt} + \frac{1}{c}U_{tt} - \frac{c}{2}U_{xx} = 0, \quad y = h \text{ boundary} \tag{27c}$$

For the FD-TD simulation of the vector Maxwell's equations, the RBC' of (26) and (27) are applied to individual Cartesian components of $\overline{I}$ or $\overline{H}$ that are located at, and tangential to, the grid boundaries.

The derivation of RBC's for the three-dimensional case follows th above development closely. The wave equation, given by

$$U_{xx} + U_{yy} + U_{zz} - \frac{1}{c^2}U_{tt} = 0 \qquad (28a$$

has the associated partial differential operator

$$L \equiv D_x^2 + D_y^2 + D_z^2 - \frac{1}{c^2}D_t^2 \qquad (28b$$

L can be factored in the manner of (23a) to provide an exact radiatio boundary operator, L^-, having the same form as that of (23b), bu with S given by

$$S = \left[\left(\frac{D_y}{D_t/c}\right)^2 + \left(\frac{D_z}{D_t/c}\right)^2\right]^{\frac{1}{2}} \qquad (28($$

Again, L^- applied to the scalar wave function, U, at the $x = 0$ gri boundary will exactly absorb a plane wave propagating toward th boundary at an arbitrary angle.

Using the Taylor series approximation of (25a), we obtain an a proximate RBC at $x = 0$ in differential-operator form

$$\left(D_x - \frac{D_t}{c} + \frac{cD_y^2}{2D_t} + \frac{cD_z^2}{2D_t}\right)U = 0 \qquad (2$$

Multiplying (29) through by D_t, and identifying the differential ope ators as partial derivatives, we obtain the corresponding approximat analytical RBC which can be numerically implemented at the $x =$ lattice boundary

$$U_{xt} - \frac{1}{c}U_{tt} + \frac{c}{2}U_{yy} + \frac{c}{2}U_{zz} = 0 \qquad (3$$

Equation (30) is a very good approximation of the exact RBC of (2 for relatively small values of S given by (28c). This is equivalent saying that (30) presents a nearly reflectionless lattice truncation f numerical plane wave modes which strike the $x = 0$ lattice bounda close to broadside. Analogous approximate, analytical RBC's can b derived for the other lattice boundaries:

$$U_{xt} + \frac{1}{c}U_{tt} - \frac{c}{2}U_{yy} - \frac{c}{2}U_{zz} = 0, \quad x = h\,\text{boundary} \tag{31a}$$

$$U_{yt} - \frac{1}{c}U_{tt} + \frac{c}{2}U_{xx} + \frac{c}{2}U_{zz} = 0, \quad y = 0\,\text{boundary} \tag{31b}$$

$$U_{yt} + \frac{1}{c}U_{tt} - \frac{c}{2}U_{xx} - \frac{c}{2}U_{zz} = 0, \quad y = h\,\text{boundary} \tag{31c}$$

$$U_{zt} - \frac{1}{c}U_{tt} + \frac{c}{2}U_{xx} + \frac{c}{2}U_{yy} = 0, \quad z = 0\,\text{boundary} \tag{31d}$$

$$U_{zt} + \frac{1}{c}U_{tt} - \frac{c}{2}U_{xx} - \frac{c}{2}U_{yy} = 0, \quad z = h\,\text{boundary} \tag{31e}$$

For the FD-TD simulation of the vector Maxwell's equations, the RBC's of (30) and (31) are applied to individual Cartesian components of $\overline{E}$ or $\overline{H}$ that are located at, and tangential to, the lattice boundaries.

Equations (26) and (27), representing approximate RBC's for a two-dimensional grid, and (30) and (31), representing approximate RBC's for a three-dimensional lattice, have been found to be very effective when implemented using the differencing scheme proposed by Mur (discussed below). These RBC's truncate an FD-TD space grid or lattice with an overall level of spurious reflections of only 1%–5% for arbitrary targets, if the outer grid or lattice planes are located 10–20 space cells from the target surface. This level of suppression of spurious reflections has been found sufficient to permit highly accurate computational modeling of scattering. For example, the radar cross section of three-dimensional targets spanning 9 wavelengths (96 space cells) has been modeled with an accuracy of 1 dB over a 40-dB dynamic range using an FD-TD space lattice having outer planes located only 0.75 wavelength (8 cells) from the target surface, as is shown in section 8.7.

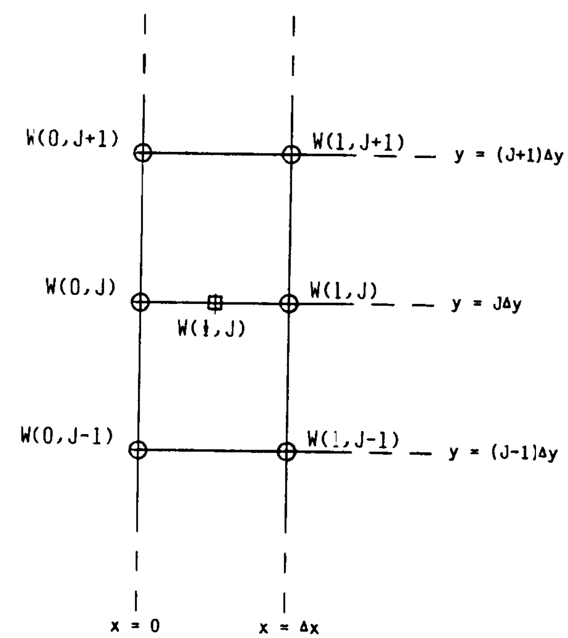

Figure 9 Points near the x=0 boundary used in the Mur differencin scheme.

c. *Mur Differencing Scheme*

A simple and successful finite-difference scheme for the two-terı Taylor series RBC's of (26), (27) and (30), (31) was introduced by Mu [11]. For clarity, this scheme is illustrated for the two-dimensional gri case at the $x = 0$ grid boundary. Referring to Fig. 9, $W^n(i,j)$ rep resents an individual Cartesian component of $\overline{E}$ or $\overline{H}$ that is locate at, and tangential to, the grid boundary at $x = 0$. The Mur schem involves implementing the partial derivatives of (26) as numerical cen tral differences expanded about the auxiliary W component, $W^n(\frac{1}{2},j)$ located one-half space cell from the grid boundary at $(0,j)$. In the firs step of the derivation of the Mur scheme, the mixed partial x and derivatives on the left hand side of (26) are written out using centra differences

$$W_{xt}\Big|_{(\frac{1}{2},j,n)} = \frac{\frac{\partial W^{n+1}}{\partial x}(\frac{1}{2},j) - \frac{\partial W^{n-1}}{\partial x}(\frac{1}{2},j)}{2\Delta t} \tag{32a}$$

$$= \frac{\left[\frac{W^{n+1}(1,j)-W^{n+1}(0,j)}{\Delta x}\right] - \left[\frac{W^{n-1}(1,j)-W^{n-1}(0,j)}{\Delta x}\right]}{2\Delta t}$$

Next, the partial t derivative on the left hand side of (26) is written out as an average of time derivatives at the adjacent points $(0,j)$ and $(1,j)$

$$W_{tt}\Big|_{(\frac{1}{2},j,n)} = \frac{1}{2}\left[\frac{\partial^2 W^n}{\partial t^2}(0,j) + \frac{\partial^2 W^n}{\partial t^2}(1,j)\right]$$

$$= \frac{1}{2}\left[\frac{W^{n+1}(0,j) - 2W^n(0,j) + W^{n-1}(0,j)}{\Delta t^2}\right. \tag{32b}$$

$$\left. + \frac{W^{n+1}(i,j) - 2W^n(1,j) + W^{n-1}(1,j)}{\Delta t^2}\right]$$

And, the partial y derivative on the left hand side of (26) is written out as an average of y derivatives at the adjacent points $(0,j)$ and $(1,j)$

$$W_{yy}\Big|_{(\frac{1}{2},j,n)} = \frac{1}{2}\left[\frac{\partial^2 W^n}{\partial y^2}(0,j) + \frac{\partial^2 W^n}{\partial y^2}(1,j)\right]$$

$$= \frac{1}{2}\left[\frac{W^n(0,j+1) - 2W^n(0,j) + W^n(0,j-1)}{\Delta y^2}\right. \tag{32c}$$

$$\left. + \frac{W^n(1,j+1) - 2W^n(1,j) + W^n(1,j-1)}{\Delta y^2}\right]$$

Substituting the finite-difference expressions of (32) into (26) and ing for $W^{n+1}(0,j)$, we obtain the following time-stepping algorith components of W along the $x = 0$ grid boundary which implen the Taylor series RBC of (26)

$$W^{n+1}(0,j) = -W^{n-1}(1,j) + \frac{c\Delta t - \Delta x}{c\Delta t + \Delta x}[W^{n+1}(1,j) + W^{n-1}(0,$$

$$+ \frac{2\Delta x}{c\Delta t + \Delta x}[W^n(0,j) + W^n(1,j)]$$

$$+ \frac{(c\Delta t)^2 \Delta x}{2\Delta y^2(c\Delta t + \Delta x)}[W^n(0,j+1) - 2W^n(0,j) + W^n(0,j-$$

$$+ W^n(1,j+1) - 2W^n(1,j) + W^n(1,j-1)]$$

For a square grid, $\Delta x = \Delta y = \delta$, and the Mur RBC at x = 0 ca written as

$$W^{n+1}(0,j) = -W^{n-1}(1,j) + \frac{c\Delta t - \delta}{c\Delta t + \delta}[W^{n+1}(1,j) + W^{n-1}(0,j)$$

$$+ \frac{2\delta}{c\Delta t + \delta}[W^n(0,j) + W^n(1,j)]$$

$$+ \frac{(c\Delta t)^2}{2\delta(c\Delta t + \delta)}[W^n(0,j+1) - 2W^n(0,j) + W^n(0,j-1)$$

$$+ W^n(1,j+1) - 2W^n(1,j) + W^n(1,j-1)]$$

Analogous finite-difference expressions for the Mur RBC at each of the other grid boundaries, $x = h, y = 0$, and $y = h$, can be derived by substituting into (27a), (27b), and (27c), respectively, in the same manner. More simply, these Mur RBC's can be obtained by inspection from (33) and (34) using coordinate symmetry arguments.

The derivation of Mur finite-difference expressions for the radiation boundary condition in three dimensions follows the above development closely. For clarity, the Mur scheme is again illustrated at the $x = 0$ lattice boundary, with Fig. 9 now representing individual Cartesian components of $\overline{E}$ or $\overline{H}$ located in lattice plane $z = k\Delta z$. Here, the Mur scheme involves implementing the partial derivatives of (30) as numerical central differences expanded about the auxiliary W component, $W^n(\frac{1}{2}, j, k)$, located one-half space cell from the grid boundary at $(0, j, k)$. The partial derivatives, W_{xt}, W_{tt}, and W_{yy} are identical in form to (32a), (32b), and (32c), respectively, and are evaluated in lattice plane $z = k\Delta z$. The partial derivative, W_{zz}, is expressed as an average of z derivatives at the adjacent points $(0, j, k)$ and $(1, j, k)$

$$W_{zz}\Big|_{(\frac{1}{2},j,k,n)} = \frac{1}{2}\left[\frac{\partial^2 W^n}{\partial z^2}(0,j,k) + \frac{\partial^2 W^n}{\partial z^2}(1,j,k)\right]$$

$$= \frac{1}{2}\left[\frac{W^n(0,j,k+1) - 2W^n(0,j,k) + W^n(0,j,k-1)}{\Delta z^2}\right.$$

$$\left.+ \frac{W^n(1,j,k+1) - 2W^n(1,j,k) + W^n(1,j,k-1)}{\Delta z^2}\right] \qquad (35)$$

Substituting these finite-difference expressions into (30) and solving for $W^{n+1}(0, j, k)$, we obtain the following time-stepping algorithm for components of W along the $x = 0$ lattice boundary which implements the Taylor series RBC of (30)

$$W^{n+1}(0,j,k) = -W^{n-1}(1,j,k) + \frac{c\Delta t - \Delta x}{c\Delta t + \Delta x}[W^{n+1}(1,j,k)$$

$$+ W^{n-1}(0,j,k)] + \frac{2\Delta x}{c\Delta t + \Delta x}[W^n(0,j,k) + W^n(1,j,k)]$$

$$+ \frac{(c\Delta t)^2\Delta x}{2\Delta y^2(c\Delta t + \Delta x)}[W^n(0,j+1,k) - 2W^n(0,j,k) + W^n(0,j-1,$$

$$+ W^n(1,j+1,k) - 2W^n(1,j,k) + W^n(1,j-1,k)]$$

$$+ \frac{(c\Delta t)^2\Delta x}{2\Delta z^2(c\Delta t + \Delta x)}[W^n(0,j,k+1) - 2W^n(0,j,k) + W^n(0,j,k-$$

$$+ W^n(1,j,k+1) - 2W^n(1,j,k) + W^n(1,j,k-1)]$$

(3

For a cubic lattice, $\Delta x = \Delta y = \Delta z = \delta$, and the Mur RBC at $x =$ can be written as

$$W^{n+1}(0,j,k) = -W^{n-1}(1,j,k) + \frac{c\Delta t - \delta}{c\Delta t + \delta}[W^{n+1}(1,j,k)$$

$$+ W^{n-1}(0,j,k)] + \frac{2\delta}{c\Delta t + \delta}[W^n(0,j,k) + W^n(1,j,k)]$$

$$+ \frac{(c\Delta t)^2}{2\delta(c\Delta t + \delta)}[W^n(0,j+1,k) - 4W^n(0,j,k) + W^n(0,j-1,k)$$

$$+ W^n(1,j+1,k) - 4W^n(1,j,k) + W^n(1,j-1,k) + W^n(0,j,k+1)$$

$$+ W^n(0,j,k-1) + W^n(1,j,k+1) + W^n(1,j,k-1)] \qquad (37)$$

Analogous finite-difference expressions for the Mur RBC at each of the other lattice boundaries, $x = h, y = 0, y = h, z = 0$, and $z = h$, can

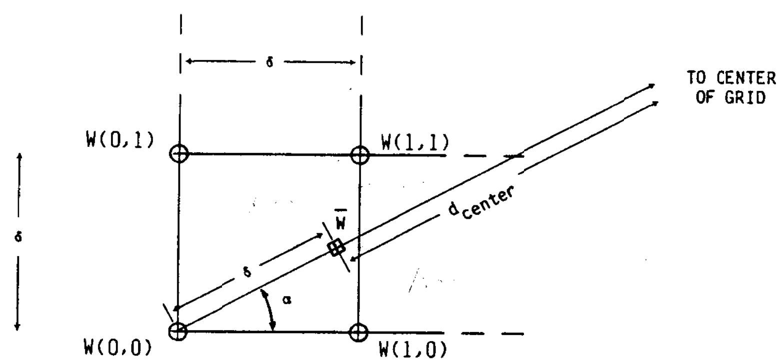

Figure 10 Points near the $x = 0$, $y = 0$ grid corner used in the special corner radiation boundary condition (square grid case).

be derived by substituting into (31a)–(31e), respectively, in the same manner. More simply, these Mur RBC's can be obtained by inspection from (36) and (37) using coordinate symmetry arguments.

d. Special Corner RBC

Upon inspecting (33) and (36), it is clear that the Mur finite-difference scheme for the two-term Taylor series RBC's cannot be implemented for field components located at grid corners, since some of the necessary field data used in the Mur expressions at these points is outside of the grid and not available. It is necessary to implement a special corner radiation boundary condition at these points which: (1) utilizes available field data in the grid; (2) yields acceptably low levels of reflection of outgoing numerical wave modes; and (3) is numerically stable.

Figure 10 illustrates the two-dimensional grid geometry for a simple and stable special corner RBC used successfully since 1982 for a wide variety of two- and three-dimensional FD-TD simulations beginning with that of [12]. The special corner RBC uses a first-order accurate propagation argument wherein the value of a corner field component, for example $W(0,0)$, is taken to be just the time-retarded value of an interior field, $\overline{W}$, located along a radial line connecting the corner point to the center of the grid. This propagation argument assumes that each scattered numerical wave mo... is radially out... at the corner point. For simplicity, we further assume that the rel... $c\Delta t = \delta/2$ is maintained, so that if $\overline{W}$ is located exactly one cell-w... δ, inward along the radial line, the time retardation of the out... numerical wave in propagating from $\overline{W}$ to $W(0,0)$ is exactly two steps. Overall, the special corner RBC is given by

$$W^{n+1}(0,0) = f_{\text{radial}} \cdot \overline{W}^{n-1}$$

where f_{radial} is the attenuation factor for the radially outgoing w... In two dimensions, we have from Fig. 10

$$f_{\text{radial}} = \left(\frac{d_{\text{center}}}{d_{\text{center}} + 1}\right)^{\frac{1}{2}}$$

$$\begin{aligned}\overline{W}^{n-1} &= (1 - \sin\alpha)(1 - \cos\alpha)\, W^{n-1}(0,0) \\ &+ (1 - \sin\alpha)\cos\alpha\, W^{n-1}(1,0) \\ &+ \sin\alpha(1 - \cos\alpha)\, W^{n-1}(0,1) \\ &+ \sin\alpha\, \cos\alpha\, W^{n-1}(1,1)\end{aligned}$$

where d_{center} is the radial distance, in cell-widths, from $\overline{W}$ to the ce... of the grid, and α is the azimuth angle of the radial line at $W(0$... Note that the value of $\overline{W}^{n-1}$ is determined by simple linear inter... lation of the four surrounding field values, including $W(0,0)$, at t... step $n - 1$. Extension to three dimensions is straightforward, yield... for $W^{n+1}(0,0,k)$

$$f_{\text{radial}} = \left(\frac{d_{\text{center}}}{d_{\text{center}} + 1}\right) \qquad (4...$$

$$\overline{W}^{n-1} = (1-\sin\beta)(1-\cos\beta\sin\alpha)(1-\cos\beta\cos\alpha)\,\overline{W}^{n-1}(0,0,k)$$
$$+ (1-\sin\beta)(1-\cos\beta\sin\alpha)\cos\beta\cos\alpha\,\overline{W}^{n-1}(1,0,k)$$
$$+ (1-\sin\beta)\cos\beta\sin\alpha(1-\cos\beta\cos\alpha)\,\overline{W}^{n-1}(0,1,k)$$
$$+ (1-\sin\beta)\cos^2\beta\sin\alpha\cos\alpha\,\overline{W}^{n-1}(1,1,k)$$
$$+ \sin\beta(1-\cos\beta\sin\alpha)(1-\cos\beta\cos\alpha)\,\overline{W}^{n-1}(0,0,k+1)$$
$$+ \sin\beta(1-\cos\beta\sin\alpha)\cos\beta\cos\alpha\,\overline{W}^{n-1}(1,0,k+1)$$
$$+ \sin\beta\cos\beta\sin\alpha(1-\cos\beta\cos\alpha)\,\overline{W}^{n-1}(0,1,k+1)$$
$$+ \sin\beta\cos^2\beta\sin\alpha\cos\alpha\,\overline{W}^{n-1}(1,1,k+1) \qquad (40b)$$

where β is the elevation angle of the radial line at $W(0,0,k)$. Here, note that the value of $\overline{W}^{n-1}$ is determined by simple linear interpolation of the eight surrounding field values, including $W(0,0,k)$, at time step $n-1$. Special RBC's for field components along the other corners of a three-dimensional lattice can be obtained by inspection from (40) using coordinate symmetry arguments, and properly defining angles α and β.

e. *Generalized and Higher-Order RBC's*

Trefethen and Halpern [18] proposed a generalization of the two-term Taylor series approximation to the radical in (23b), considering the use of the rational function approximation

$$\sqrt{1-S^2} \simeq r(S) = \frac{p_m(S)}{q_n(S)} \qquad (41)$$

on the interval $[-1,1]$, where p_m and q_n are polynomials in S of degree m and n, respectively; and $r(S)$ is said to be of type (m,n). With $S = cD_y/D_t$, the $[-1,1]$ approximation interval on S is equivalent to approximation of the exact one-way wave equation of (24) along the $x=0$ grid boundary for the range of incident wave angles $\theta = -90°$ to $\theta = +90°$.

For example, by specifying $r(S)$ as a general (2,0) approximant, the radical is approximated by an interpolating polynomial of the form

$$\sqrt{1-S^2} \simeq p_0 + p_2 S^2 \qquad (42a)$$

resulting in the general second-order, approximate, analytical Rl

$$U_{xt} - \frac{p_0}{c} U_{tt} - p_2 c\, U_{yy} = 0 \qquad ($$

The choice of the coefficients, p_0 and p_2, is determined by the me of interpolation that is used. Standard techniques such as Padé, l square, or Chebyshev approximation are applied with the goal c terpolating the radical optimally over the $[-1,1]$ range of S, the producing an approximate RBC whose performance is good over a range of incident wave angles. Mur's two-term Taylor series ap imation of (25a) is now seen in a more general sense as a Padé (interpolant, i.e., with coefficients $p_0 = +1$ and $p_2 = -\frac{1}{2}$ in (42b).

Higher-order rational function approximations to the $\sqrt{1}$ term were proposed in [18] as a means to derive an approximate l having good accuracy over a wider range of incident wave angles t that possible with (42). For example, the use of the general type (rational function

$$\sqrt{1-S^2} \simeq \frac{p_0 + p_2 S^2}{q_0 + q_2 S^2} \qquad (\cdot$$

gives the general third-order, approximate, analytical RBC

$$q_0\, U_{xtt} + q_2 c^2\, U_{xyy} - \frac{p_0}{c}\, U_{ttt} - p_2 c\, U_{tyy} = 0 \qquad (4$$

Appropriate selection of the p and q coefficients in (43) produces ious families of RBC's, as suggested in [18]. For example, $q_0 = p$ $1, p_2 = -\frac{3}{4}$, and $q_2 = -\frac{1}{4}$ gives a Padé (2,2) approximation in (4 with the resulting RBC functioning better than (26) for numer waves impacting the $x = 0$ grid boundary at all angles. Figure depicts two ways of quantifying the improved performance of the P (2,2) RBC relative to Mur's Padé (2,0) condition [19,20]. In Fig. 11(the theoretical numerical wave reflection coefficient is plotted as a fu tion of angle of incidence for the two Padé RBC's. In Fig. 11(b), the tal squared-error in a test grid due to imperfect RBC's (generated b smooth, finite-duration, cylindrical outgoing pulse centered in the gr is plotted as a function of time-step number for the two RBC's. We that the theoretical improvement of reflection coefficient for the Pa (2,2) RBC (most pronounced near normal incidence, 0°) translates about a 10:1 actual reduction of total error energy in the test g as the outgoing pulse propagates radially through the Cartesian g

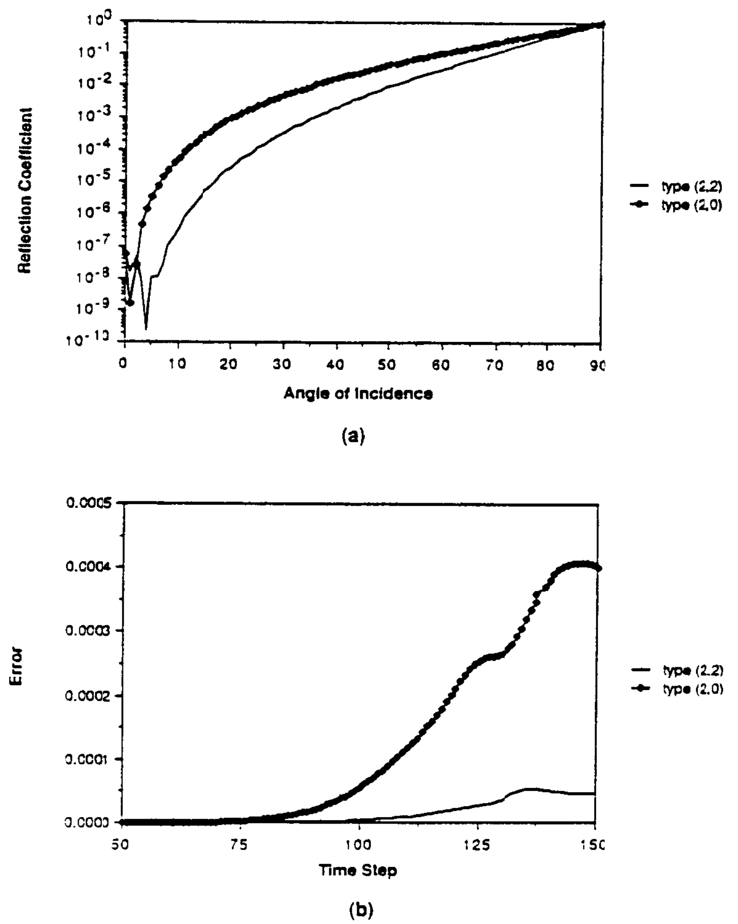

Figure 11 Improved performance of the Padé (2,2) RBC relative to the Mur condition: (a) Theoretical reflection coefficient; (b) Total squared-error in a test grid [19,20].

boundaries. This reduction in grid noise is worthwhile, permitting in principle extension of FD-TD modeling to targets having correspondingly reduced radar cross section. As a consequence, the Padé (2,2) RBC and similar higher-order conditions are currently being studied as potential replacements for the long-used Mur RBC.

8.6 FD-TD Modeling Validations in 2-D

Analytical and code-to-code validations have been obtained tive to FD-TD modeling of electromagnetic wave scattering for a variety of canonical two-dimensional structures. Both convex an entrant (cavity- type) shapes have been studied; and structure mat compositions have included perfect conductors, homogeneous and i mogeneous lossy dielectrics, and anisotropic dielectric and perme media. Selected validations will be reviewed here.

a. Square Metal Cylinder, TM Polarization

Here, we consider the scattering of a TM-polarized plane v obliquely incident upon a square metal cylinder of electrical size $k_($ 2, where s is the side width of the cylinder [12]. The square FD grid cell size is set equal to $s/20$, and the grid truncation (radia boundary) is located at a uniform distance of 20 cells from the cyli surface.

Figure 12 compares the magnitude and phase of the cylinder face electric current distribution computed using FD-TD to that c puted using a benchmark code which solves the frequency-domain face electric field integral equation (EFIE) via the method of mom (MOM). The MOM code assumes target symmetry and discretizes half of the cylinder surface with 84 divisions. The FD-TD comp surface current is taken as $\hat{n} \times \overline{H}_{tan}$, where $\hat{n}$ is the unit normal ve at the cylinder surface, and $\overline{H}_{tan}$ is the FD-TD value of the magn field vector component in free space immediately adjacent to the cy der surface. From Fig. 12, we see that the magnitude of the FD- computed surface current agrees with the MOM solution to better t $\pm 1\%$ ($\pm$ 0.09 dB) at all comparison points more than 2 FD-TD from the cylinder corners (current singularities). The phase of the TD solution agrees with the MOM solution to within $\pm 3°$ at virtu every comparison point, including the shadow region.

b. Circular Muscle-Fat Layered Cylinder, TE Polarization

Here, we consider the penetration of a TE-polarized plane w into a simulated biological tissue structure represented by a 15 cm dius muscle-fat layered cylinder [21]. The inner layer (radius = 7.9 is assumed to be comprised of muscle having a relative permittivit 72 and conductivity of 0.9 S/m. The outer layer is assumed to